JPhys Materials

OPEN ACCESS

RECEIVED
4 October 2018

REVISED
19 February 2019

ACCEPTED FOR PUBLICATION
25 February 2019

PUBLISHED
26 March 2019

PAPER

Spatio-temporal dynamics of shift current quantum pumping by femtosecond light pulse

U Bajpai[1], **B S Popescu**[1], **P Plecháč**[2], **B K Nikolić**[1,3], **L E F Foa Torres**[4], **H Ishizuka**[5] **and N Nagaosa**[3,5]

[1] Department of Physics and Astronomy, University of Delaware, Newark, DE 19716-2570, United States of America
[2] Department of Mathematical Sciences, University of Delaware, Newark, DE 19716, United States of America
[3] RIKEN Center for Emergent Matter Sciences (CEMS), Wako, Saitama, 351-0198, Japan
[4] Departamento de Física, Facultad de Ciencias Físicas y Matemáticas, Universidad de Chile, Santiago, Chile
[5] Department of Applied Physics, The University of Tokyo, Bunkyo, Tokyo, 113-8656, Japan

E-mail: bnikolic@udel.edu

Keywords: ultrafast phenomena, photovoltaics, optoelectronics, nonadiabatic quantum pumping in nanostructures, time-dependent quantum transport simulations, nonlinear optics, ferroelectrics

Supplementary material for this article is available online

Abstract

Shift current—a photocurrent induced by light irradiating noncentrosymmetric materials in the absence of any bias voltage or built-in electric field—is one of the mechanisms of the so-called bulk photovoltaic effect. It has been traditionally described as a nonlinear optical response of a periodic solid to continuous wave light using a perturbative formula, which is linear in the intensity of light and which involves Berry connection describing the shift in the center of mass position of the Wannier wave function associated with the transition between the valence and conduction bands of the solid. Since shift current is solely due to off-diagonal elements of the nonequilibrium density matrix that encode quantum correlations, its peculiar space–time dynamics in response to femtosecond light pulse employed locally can be expected. To study such response requires to analyze realistic two-terminal devices, instead of traditional periodic solids, for which we choose paradigmatic Rice–Mele model sandwiched between two metallic electrodes and apply to it time-dependent nonequilibrium Green function algorithms scaling linearly in the number of time steps and capable of treating nonperturbative effects in the amplitude of external time-dependent fields. This reveals novel features: *superballistic* transport, signified by time dependence of the displacement, $\sim t^{\nu}$ with $\nu > 1$, of the photoexcited charge carriers from the spot where the femtosecond light pulse is applied toward the electrodes; and photocurrent quadratic in light intensity at subgap frequencies of light due to *two-photon absorption* processes that were missed in previous perturbative analyses. Furthermore, frequency dependence of the DC component of the photocurrent reveals shift current as a realization of nonadiabatic quantum charge pumping enabled by *breaking of left–right symmetry* of the device structure. This demonstrates that a much wider class of systems, than the usually considered polar noncentrosymmetric bulk materials, can be exploited to generate nonzero DC component of photocurrent in response to unpolarized light and optimize shift-current-based solar cells and optoelectronic devices.

1. Introduction

The conventional photovoltaics is based on semiclassical transport of electrons and holes excited by light and separated by the built-in electric field within a *pn*-junction where careful control of disorder and flow of light inside a solar cell is required to reduce entropic energy losses [1]. An alternative is distinctly different physical mechanism—the so-called bulk photovoltaic effect (BPVE) [2]—which appears in *noncentrosymmetric* materials [3], such as ferroelectrics with nonzero electric polarization. The BPVE generates steady-state photocurrent and the above band-gap photovoltage as the signatures of *nonlinear optical response*. The BPVE can

be substantially enhanced in ferroelectric thin films [4], and potentially even more in Weyl semimetals [5]. However, photocurrent generated by BPVE in a closed circuit remains small compared to *pn*-junctions. This has ignited renewed experimental [4, 6–11] and theoretical [12–18] interest in BPVE with the ultimate goal [15] to optimize its power conversion efficiency.

Aside from potential applications, the nonlinear optical response has also emerged [19, 20] as a sensitive probe of local (or geometric) properties of quantum wavefunction in noncentrosymmetric materials, including topological insulators [21] and Weyl semimetals [5, 22, 23]. The geometric properties of wavefunction are encoded by the Berry-phase-concepts, such as Berry connection and Berry curvature, which govern DC component of injection current or shift current driven by high-energy electric fields of circularly- or linearly-polarized light, respectively. This is somewhat surprising since such fields induce interband transitions in which electronic wavefunctions are not confined to specific bands and adiabatic condition is violated [19, 20].

The BPVE can have contributions from different processes [2, 9, 24, 25], where the most intensely studied are: (i) the shift current contribution, traditionally explained as a shift in real space following the carrier interband transition [24–26]; and (ii) the ballistic current contribution due to intraband transition of hot photoelectrons with asymmetric momentum distribution during which they lose their energy to descend to the bottom of conduction band while shifting in real space [2]. The shift current has attracted particular attention due to its inherently quantum-mechanical nature involving *phase-coherent evolution* of electron and hole wave functions. This makes possible rapid propagation of charge carriers toward the electrodes, thereby minimizing carrier recombination (that reduces the magnitude of conventional photocurrent) and energy losses due to carrier-phonon scattering [25]. For example, very recent experiments [10, 11] shining a laser spot onto the middle of the sample have detected shift current across the whole sample, independently of the position and the width of the excited region, and extracted it $\sim$100 μm away from the excited region.

The widely used [12–17] 'standard model'[25, 26] for computing the magnitude of shift current is based on a perturbative expansion which yields its DC component

$$J_p(\omega) = \sigma_{pqr}(\omega) E_q(\omega) E_r(\omega), \tag{1}$$

as a second-order nonlinear optical response to electric field $E_q(\omega)$ of the incident monochromatic light of frequency ω and polarization in the q-direction. The unpolarized sunlight is modeled by averaging $\sigma_{pqr}(\omega)$ over different polarizations. Thus, equation (1) can only describe photocurrent linear in intensity, as typically encountered also in conventional photovoltaics [27, 28]. The third-rank tensor $\sigma_{pqr}(\omega)$ can be expressed as a product of two terms carrying intuitive meaning [12, 15, 17]—diagonal imaginary part of the dielectric function, which is proportional to the density of states (DOS); and the so-called shift vector (of magnitude [2] 10–100 nm) as the average distance traveled by coherent photoexcited charge carriers during their lifetime. The shift vector depends on the Berry connection [19, 20] of the Bloch energy bands of an infinite periodic crystal and it is, therefore, an intrinsic property of the material insensitive to elastic and inelastic scattering processes [25].

However, the 'standard model' tailored for infinite periodic crystals cannot be used to compute open-circuit photovoltage, as one of the key factors determining the power conversion efficiency [14], or examine the effect of the electrodes on the measured photocurrent. Furthermore, it cannot describe photocurrent response to a femtosecond light pulse applied locally to a finite-size open quantum system attached to macroscopic reservoirs, as illustrated in figure 1. On the other hand, such setups have recently become popular in experiments [6–8, 10, 11] aiming to understand: (i) how fast shift current responds to light and how fast it propagates toward the metallic electrodes [10, 11]; (ii) how it develops spatially [6, 7]; and (iii) how it can deviate [8] from the linear dependence on the intensity of light or, equivalently, quadratic dependence on the electric field as in equation (1).

In this study, we apply time-dependent nonequilibrium Green function (TDNEGF) formalism [29, 30] to compute in numerically exact and, therefore, *nonperturbative* fashion temporal and spatial development of photocurrent induced by light pulse of duration $\sigma_{\rm light}$ and center frequency Ω irradiating Rice–Mele tight-binding (TB) chain with broken inversion symmetry. To mimic recent experiments [10], we use chain of length $N_{\rm RM} > N_{\rm RM}^{\rm light}$ whose middle $N_{\rm RM}^{\rm light}$ sites are irradiated by light pulse. The Rice–Mele TB chain is attached to two semi-infinite leads (modeled also as TB chains) to form a realistic two-terminal device geometry illustrated in figure 1. This makes it possible to study how fast photocurrent induced in the middle part of such device propagates toward its electrodes, and how much of photoexcited electrons can eventually be extracted into the electrodes.

The paper is organized as follows. In section 2, we introduce the Rice–Mele Hamiltonian and the DOS and DC transport properties of the devices in figure 1. This section also explains TDNEGF algorithms for constructing time-dependent nonequilibrium density matrix of this device viewed as an open quantum system. Section 3.1 discusses two-photon versus one-photon absorption mechanism which generate subgap versus above-the-gap photocurrent in this device. In section 3.2 we demonstrate shift photocurrent as a realization of nonadiabatic quantum charge pumping in two-terminal devices with broken left–right-symmetry. Section 3.3

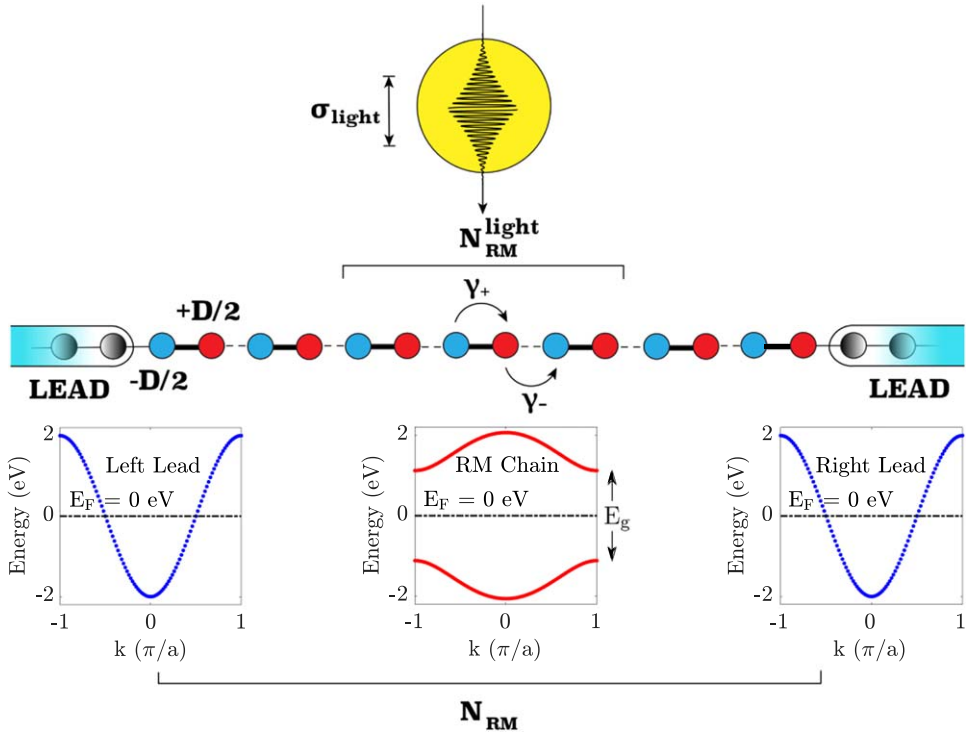

Figure 1. Schematic view of a two-terminal device where photocurrent is generated by a femtosecond light pulse of duration $\sigma_{\rm light}$ in the absence of any DC bias voltage between its leads. The central region composed of $N_{\rm RM}$ sites is modeled by noncentrosymmetric Rice–Mele TB Hamiltonian in equation (2) with alternating hoppings and staggered on-site potential illustrated. It is attached to two-semi infinite NM leads modeled as TB chains with uniform hopping and zero on-site potential. The incident light pulse is assumed to couple only to $N_{\rm RM}^{\rm light} < N_{\rm RM}$ sites in the middle of Rice–Mele central region. The insets below the device show gapless band structure of NM leads, as well as band structure of an infinite Rice–Mele TB chain with an energy gap E_g between the valence and conduction bands. The Fermi energy of electrons in the NM leads is chosen as $E_F = 0$ eV, and it falls in the cente of the gap E_g, as marked in all three insets.

discusses how fast photoexcited charge carriers propagate from irradiated region of the device toward the electrodes, with additional insight provided as two movies in the supplemental material, available online at stacks.iop.org/JPMATER/2/025004/mmedia[6]. The role of quantum coherence in generation of photoexcited nonequilibrium charge density is rigorously discussed in section 3.4 by analyzing contributions to it arising from off-diagonal elements of time-dependent nonequilibrium density matrix. We conclude in section 4.

2. Models and methods

2.1. Rice–Mele Hamiltonian with coupling to a light pulse

The Rice–Mele Hamiltonian [31], as a paradigmatic model employed in shift current studies [14, 16–18], is a one-dimensional model of ferroelectricity along the polar axis

$$\hat{H}_{\rm RM} = \sum_n \left(-\gamma - \frac{B}{2}(-1)^n\right)(\hat{c}_{n+1}^\dagger \hat{c}_n + \hat{c}_n^\dagger \hat{c}_{n+1}) + \frac{D}{2}\sum_n (-1)^n \hat{c}_n^\dagger \hat{c}_n, \tag{2}$$

whose parameters have been tuned to capture electronic structure of realistic materials like polyacetylene, $BaTiO_3$ and monochalcogenides [16, 17]. Here $\hat{c}_n^\dagger$ ($\hat{c}_n$) creates (annihilates) electron in s-wave orbital $|n\rangle$ centered at site n; $\gamma_+ = -\gamma + B/2$ and $\gamma_- = -\gamma - B/2$ are the alternating hoppings between the nearest neighbor sites with B parameterizing the dimerization of the chain; and $\pm D/2$ is the staggered on-site potential. The unit cell of Rice–Mele TB chain of size $2a$ contains two sites, and inversion symmetry is broken by [14] $B \neq 0$ and $D \neq 0$. In order to mimic devices used to extract shift current in recent experiments [10, 11], we attach Rice–Mele TB chain to two semi-infinite normal metal (NM) leads depicted in figure 1, which are modeled by the same TB Hamiltonian in equation (2) but with $B = D = 0$. We set $\gamma = 1$ eV in both the NM leads and in the Rice–Mele central region where $B = D = 1$ eV is chosen. The NM leads terminate in the left (L) and right (R) macroscopic reservoirs whose chemical potentials are identical in the absence of DC bias voltage

[6] See supplemental material for two movies, accompanying figure 5(d), which show time evolution of spatial profiles of local bond photocurrent $I_{n\to m}(t)$ in clean and diffusive two-terminal devices. The movies also include local bond current from the last site of the left NM lead toward the first site of Rice–Mele TB chain, as well as from the last site of Rice–Mele TB chain toward first site of the right NM lead.

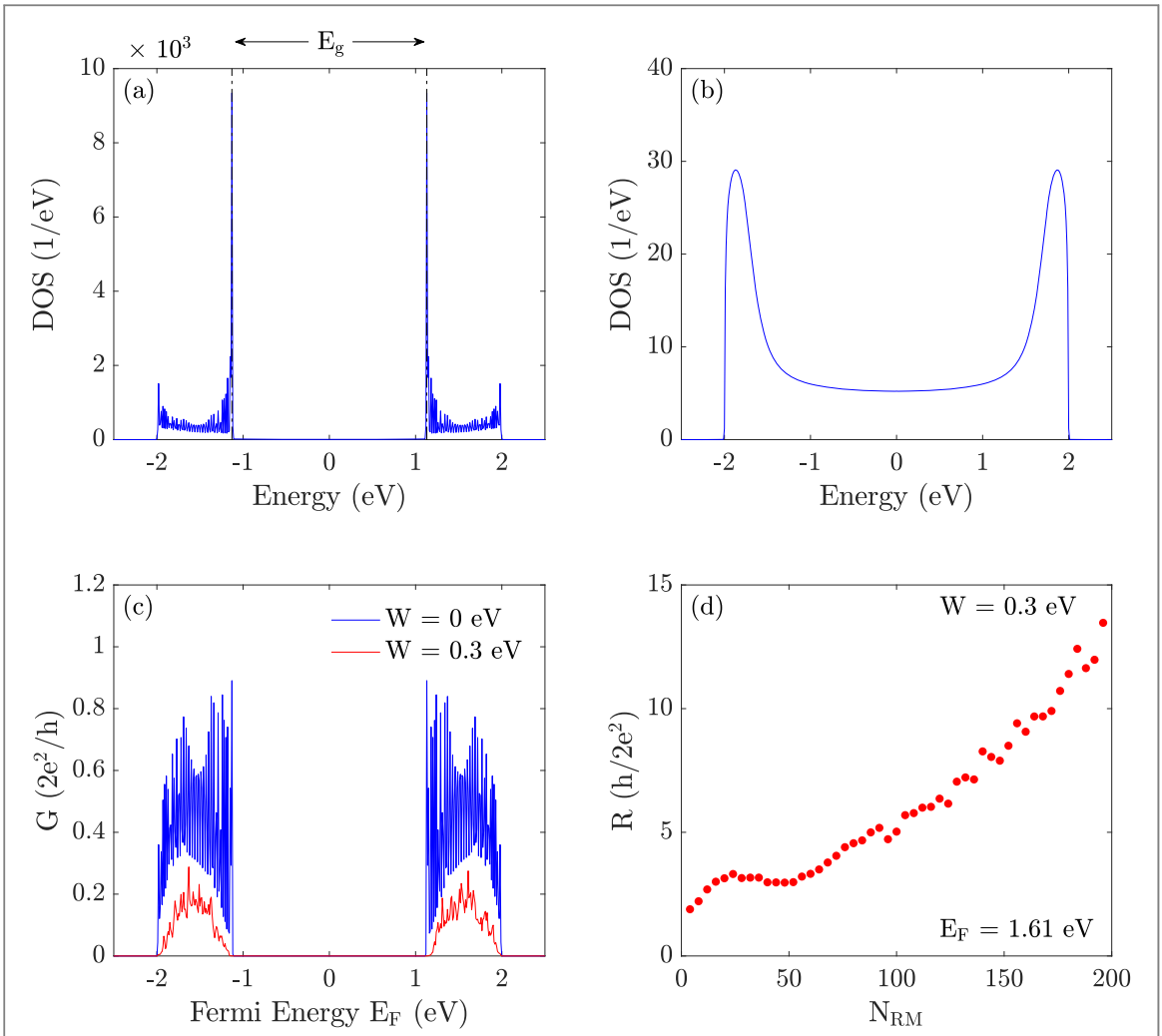

Figure 2. The DOS of the device in figure 1 with clean central region of length: (a) $N_{\rm RM} = 100$; and (b) $N_{\rm RM} = 4$ sites. The energy gap in the DOS in panel (a) is $E_g \approx 2.28$ eV. (c) The two-terminal linear-response conductance G of the device in figure 1 with $N_{\rm RM} = 100$ which is clean ($W = 0$ eV), or disordered ($W = 0.3$ eV) due to a uniform random variable $\in[-W/2, W/2]$ added onto the staggered on-site potential in equation (2). Panel (d) shows scaling of the two-terminal resistance $R = 1/G$ with $N_{\rm RM}$ at the Fermi energy $E_F = 1.61$ eV and for the same disorder strength $W = 0.3$ eV used in panel (c). The geometric disorder averaging to obtain typical G in panel (c) is performed over 25 configurations, and for typical R in panel (d) it is performed over 10^3 configurations.

and chosen as $\mu_L = \mu_R = 0$ eV, so that electrons in NM leads are at the Fermi energy $E_F = 0$ eV (which is band center of the NM leads).

For a sufficiently long Rice–Mele TB chain, this device exhibits an energy gap $E_g \approx 2.28$ eV in the DOS (figure 2(a)). We also consider gapless device where the gap of short Rice–Mele TB chain is filled with evanescent wave functions injected by the NM leads (figure 2(b)). Adding on-site disorder, modeled as a uniform random variable $\in[-W/2, W/2]$, reduces the van Hove singularities in the DOS at the gap edges while keeping finite two-terminal conductance G outside of the gap (figure 2(c)). That is, the scaling of the corresponding two-terminal resistance $R = 1/G$ in figure 2(d) with $N_{\rm RM}$ shows that for chosen $W = 0.3$ eV and $N_{\rm RM} = 100$ the device is outside of the Anderson localization regime. This setup makes it possible to quantify how fast nonequilibrium photoexcited charge carriers propagate across diffusive TB chain toward the NM leads. We compute G as a linear response to small DC bias voltage between the NM leads using the zero-temperature Landauer formula $G(E_F) = \frac{2e^2}{h} T(E_F)$, where $T(E_F)$ is the transmission function at the Fermi energy E_F.

The light pulse is described by the vector potential $\mathbf{A}(t) = A_{\rm max} \exp[-(t - t_p)^2 / (2\sigma_{\rm light}^2)] \sin(\Omega t) \mathbf{e}_x$ with a Gaussian shaped function for a pulse of duration $\sigma_{\rm light}$, centered at time t_p and center frequency Ω. Here $\mathbf{e}_x$ is the unit vector along the direction of TB chain, pointing toward the right NM lead in figure 1, which describes one of the two possible linear polarization of incident light. The corresponding electric field is $\mathbf{E} = -\partial \mathbf{A}/\partial t$. We neglect the relativistic magnetic field of the laser pulse, so that electronic spin degree of freedom maintains its degeneracy and it is excluded from our analysis. The vector potential couples to an electron via the Peierls substitution in equation (2)

$$\hat{c}_n^\dagger \hat{c}_{n+1} \mapsto \hat{c}_n^\dagger \hat{c}_{n+1} \times \exp\{iz_{\max} \exp[-(t-t_p)^2/(2\sigma_{\text{light}}^2)] \sin(\Omega t)\}, \tag{3}$$

applied only to $N_{\text{RM}}^{\text{light}} < N_{\text{RM}}$ sites in the middle of Rice–Mele TB chain, as denoted in figure 1. Here $z_{\max} = eaA_{\max}/\hbar$ is the dimensionless parameter quantifying maximum amplitude of the pulse.

2.2. TDNEGF algorithms

To compute local charges and currents driven by time-dependent terms in the Hamiltonian, we employ TDNEGF formalism which operates with two fundamental quantities [29]—the retarded $G^r_{nn'}(t, t') = -i\Theta(t-t')\langle\{\hat{c}_n(t), \hat{c}^\dagger_{n'}(t')\}\rangle$ and the lesser $G^<_{nn'}(t, t') = i\langle\hat{c}^\dagger_{n'}(t')\hat{c}_n(t)\rangle$ Green functions (GFs) describing the density of available quantum states and how electrons occupy those states, respectively. For the device in figure 1 we solve a matrix integro-differential equation [32, 33] for the time-evolution of one-particle reduced nonequilibrium density matrix, $\boldsymbol{\rho}^{\text{neq}}(t) = \mathbf{G}^<(t, t)/i$

$$i\hbar \frac{d\boldsymbol{\rho}^{\text{neq}}}{dt} = [\mathbf{H}_{\text{RM}}, \boldsymbol{\rho}^{\text{neq}}] + i \sum_{\alpha=L,R} (\boldsymbol{\Pi}_\alpha(t) + \boldsymbol{\Pi}^\dagger_\alpha(t)). \tag{4}$$

Here all bold-face quantities denote matrices of size $N_{\text{RM}} \times N_{\text{RM}}$ in the vector space defined by the central Rice–Mele region of two-terminal device in figure 1. The diagonal elements of the nonequilibrium density matrix yield the local nonequilibrium charge

$$Q_n^{\text{neq}}(t) = e(\rho_{nn}^{\text{neq}} - \rho_{nn}^{\text{eq}}), \tag{5}$$

where we subtract local charge in equilibrium. The equilibrium density matrix can be obtained either as the asymptotic limit $\boldsymbol{\rho}^{\text{neq}}(t) \to \boldsymbol{\rho}^{\text{eq}}$ after transient current dies away (and before the light pulse is applied) in the course of time evolution which couples the NM leads to the central Rice–Mele region, or by evaluating $\boldsymbol{\rho}^{\text{eq}} = -\frac{1}{\pi}\int dE\ \text{Im}\,\mathbf{G}^r(E)f(E)$ using the retarded GF in equilibrium and the Fermi function $f(E)$ of macroscopic reservoirs [35]. We explicitly confirm that both methods give identical result. The matrix

$$\boldsymbol{\Pi}_\alpha(t) = \int_{t_0}^{t} dt_2\ [\mathbf{G}^>(t, t_2)\boldsymbol{\Sigma}^<_\alpha(t_2, t) - \mathbf{G}^<(t, t_2)\boldsymbol{\Sigma}^>_\alpha(t_2, t)], \tag{6}$$

is expressed in terms of the lesser/greater GF and the corresponding lesser/greater self-energies [29] $\boldsymbol{\Sigma}^{>,<}_\alpha(t_2, t)$ whose numerical construction in order to convert equation (4) into a system of ordinary differential equations can be found in [33]. Equation (6) yields current in lead α of the device

$$I_\alpha(t) = \frac{2e}{\hbar}\,\text{Tr}\,[\boldsymbol{\Pi}_\alpha(t)], \tag{7}$$

and summing this expression with the trace of equation (4) leads to the continuity equation expressing local charge conservation in time-dependent situations. The local bond current [34] between sites n and m connected by the hopping parameter $\gamma_{nm}(t)$ is computed as

$$I_{n\to m}(t) = \frac{e}{i\hbar}[\rho_{nm}^{\text{neq}}(t)\gamma_{mn}(t) - \rho_{mn}^{\text{neq}}(t)\gamma_{nm}(t)]. \tag{8}$$

The computational complexity of TDNEGF calculations stems from the memory effect—the entire history must be stored in order to accurately evolve the GFs. For efficient calculations over long times and for large number of simulated sites, we employ newly developed TDNEGF algorithms [32, 33] which scale *linearly* [30] in the number of time steps.

3. Results and discussion

3.1. One- versus two-photon absorption mechanisms

Although electrons of any system will respond to light pulse by generating a time-dependent photocurrent, photovoltaic applications and the analysis of consequences of broken symmetry are *focused on the existence of nonzero DC component of the photocurrent*. We define DC component as

$$\langle I(t)\rangle = \frac{1}{\sigma_{\text{curr}}}\int I(t)dt, \tag{9}$$

where $\sigma_{\text{curr}} > \sigma_{\text{light}}$ is the duration of transient photocurrent, and plot it as a function of Ω in figure 3(a) for gapless and in figure 3(c) for gapped device. In gapped device nonzero $\langle I_\alpha(t)\rangle \neq 0$ appears initially at subgap frequency $\hbar\Omega \simeq \Delta/2$, which is at first sight surprising since in the 'standard model' analyses [14, 17] of an infinite Rice–Mele TB chain DC photocurrent is zero in the gap. However, it is compatible with an electron from the valence band in figure 2(a) absorbing two-photons at the same time to transition to the conduction band. Such two-photon absorption mechanism is confirmed by demonstrating in figure 3(d) scaling $\langle I_\alpha(t)\rangle \propto z^4_{\max}$ with the forth power of the electric field or, equivalently, with the square of the intensity of the light pulse. We confirm the same result using charge conserving Floquet-NEGF approach [36] (truncated to $-1, 0, +1$ Floquet

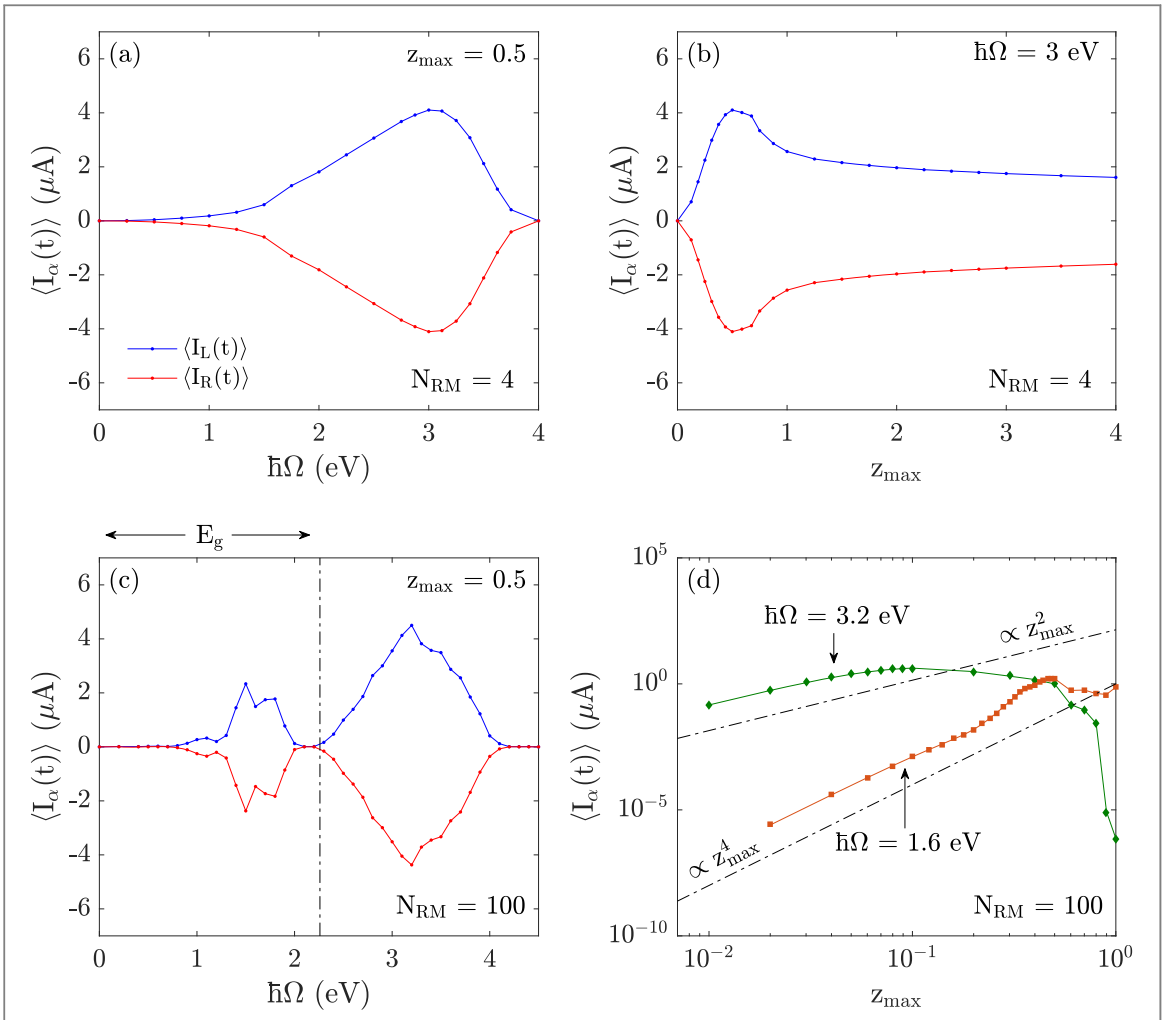

Figure 3. The DC component of photocurrent injected into *L* and *R* leads of the clean device in figure 1 as a function of (a), (c) center frequency Ω or (b), (d) maximum amplitude z_{max} of light pulse of duration $\sigma_{light} = 50$ fs. The pulse irradiates all $N_{RM} = N_{RM}^{light} = 4$ sites of Rice–Mele TB chain in (a), (b), for which the device in figure 1 is gapless with DOS shown in figure 2(b); or it irradiates $N_{RM}^{light} = 20$ middle sites of the Rice–Mele TB chain composed of $N_{RM} = 100$ sites in (c), (d), for which the device in figure 1 is gapped with the DOS shown in figure 2(a). The Fermi energy of electrons in the NM leads is chosen as $E_F = 0$ eV.

bands), where the middle of Rice–Mele TB chain is irradiated by a continuous-wave (CW) light of frequency Ω. For $\hbar\Omega \gtrsim \Delta$, the DC component of photocurrent is quadratic in the electric field in figure 3(d), $\langle I_\alpha(t)\rangle \propto z_{max}^2$, which is the signature of the usual one-photon absorption mechanism captured also by equation (1). We note that two-photon photovoltaic effect, as the nonlinear analog of conventional one-photon photovoltaic effect, is rarely observed in standard *pn*-junctions solar cells [27, 28].

To include these higher-order processes into the 'standard model' analyses requires to derive an additional expression [37] for the fifth-rank tensor $\sigma_{pqrst}(\omega)$ in order to express DC component of subgap photocurrent, $J_p(\omega) = \sigma_{pqrst}(\omega)E_q(\omega)E_r(\omega)E_s(\omega)E_t(\omega)$. On the other hand, they are naturally taken into account by our nonperturbative TDNEGF approach. Also, the TDNEGF approach applied to two-terminal devices allows one to compute the open-circuit photovoltage simply by using

$$V_{OC} = \langle I(t)\rangle R, \tag{10}$$

where the two-terminal resistance *R* (such as the one plotted in figure 2(d)) depends on the disorder and possible domain walls [38] in the central region, as well as properties of the central-region/NM-lead interfaces.

3.2. Shift current as nonadiabatic quantum charge pumping

Figure 4(a) plots time-dependence of the mean current $[I_L(t) - I_R(t)]/2$ injected into the NM leads for gapless device with $N_{RM} = 4$ sites in response to light pulse irradiating all four sites. Its DC component being nonzero in figures 3(a), (b) is in agreement with the key requirement [39–41]—*breaking of left–right symmetry*—for quantum charge pumping by a time-dependent potential. This, in turn, means breaking inversion symmetry and/or time-reversal symmetry. In the adiabatic (low frequency) regime, quantum charge pumping requires both inversion and time-reversal symmetries to be broken dynamically, such as by two spatially separated

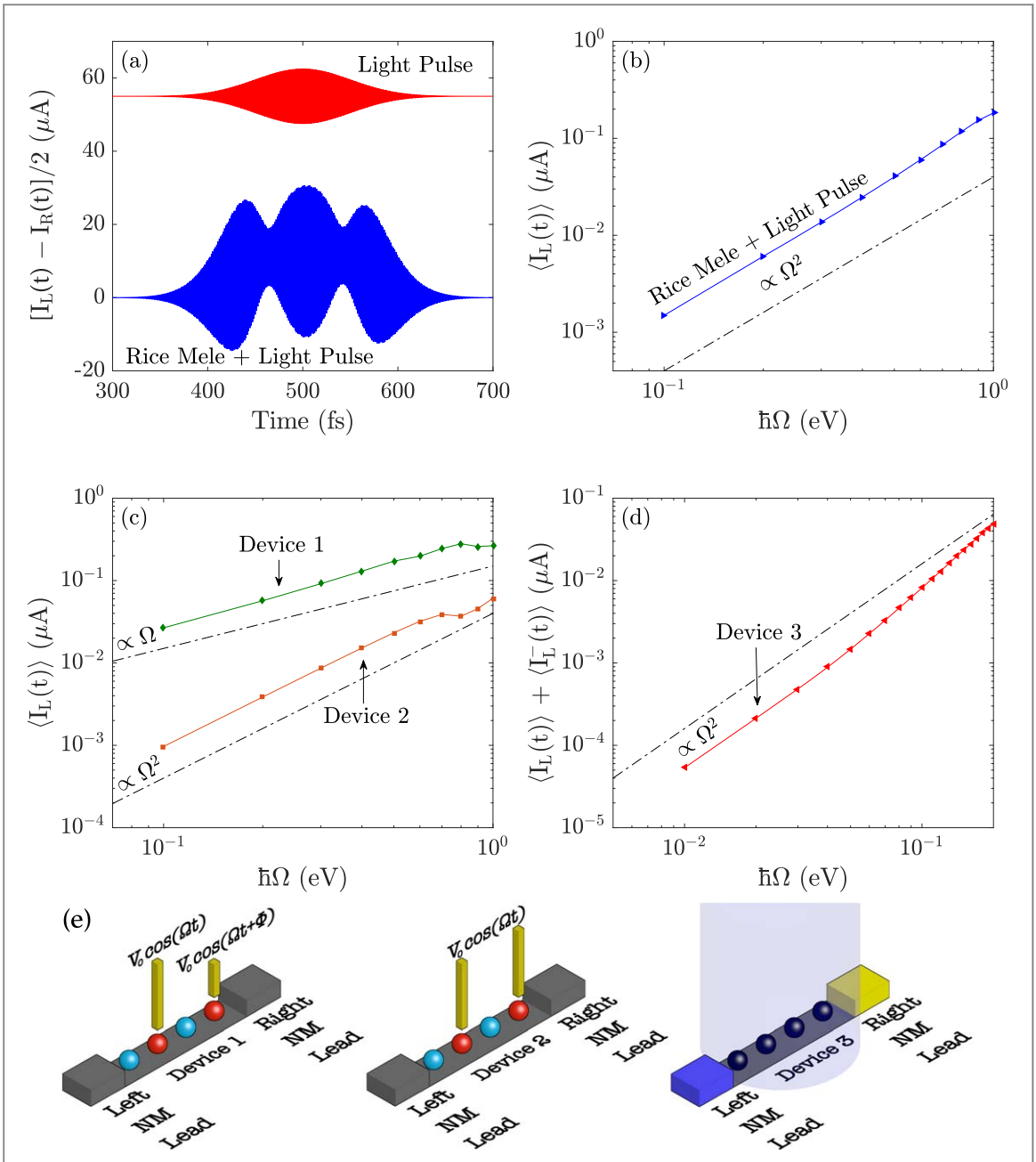

Figure 4. (a) Time dependence of photocurrent in the NM leads attached to Rice–Mele TB chain whose all $N_{\rm RM} = N_{\rm RM}^{\rm light} = 4$ sites are irradiated by femtosecond light pulse; and (b) frequency dependence of its DC component in the left NM lead. (c) Frequency dependence of the DC component of current pumped into the left NM lead of Rice–Mele TB chain with $N_{\rm RM} = 4$ sites two of which marked in panel (e) host time-dependent on-site potentials oscillating out-of-phase (Device 1) or in-phase (Device 2) with $V_0 = 1$ eV and $\Phi = -\pi/3$. (d) Frequency dependence of the DC component of photocurrent pumped into the left NM lead due to unpolarized CW light ($I_L^{+,-}(t)$ are photocurrents for two different linear polarizations of light parallel to the chain) irradiating four sites of a centrosymmetric TB chain described by $B = D = 0$ and $\gamma = 1$ eV in equation (2) but attached to two different NM leads, with hoppings $\gamma_L = 2$ eV in the left and $\gamma_R = 4$ eV in the right lead, employed to break the left–right symmetry of Device 3 in panel (e). The light pulse irradiating Rice–Mele TB chain in (a) has duration $\sigma_{\rm light} = 50$ fs, maximum amplitude $z_{\rm max} = 0.5$ and center frequency $\hbar\Omega = 3$ eV, while CW light in panel (d) has frequency $\hbar\Omega = 1$ eV and amplitude $z = 0.5$. The Fermi energy of electrons in the NM leads is chosen as $E_F = 0$ eV.

potentials oscillating out-of-phase [40], which leads to $\langle I_\alpha(t)\rangle \propto \Omega$ at low frequencies. This is confirmed in figure 4(c) for Rice–Mele TB chain driven by two on-site potentials oscillating out-of-phase (illustrated as Device 1 in figure 4(e)). In contrast, in the nonadiabatic regime [39–41], only one of those two symmetries needs to be broken and this does not have to occur dynamically. The DC component of the pumped current in the nonadiabatic regime is [41, 42] $\langle I_\alpha(t)\rangle \propto \Omega^2$ at low frequencies, as confirmed in figure 4(b) for Rice–Mele TB chain driven by light pulse from panel (a), as well as in figure 4(c) for Rice–Mele TB chain driven by two on-site potentials oscillating in-phase and illustrated as Device 2 in figure 4(e).

We note that previous theoretical analyses [14] of shift current in bulk materials have concluded that those with broken inversion symmetry but without electric polarization generate DC component of photocurrent

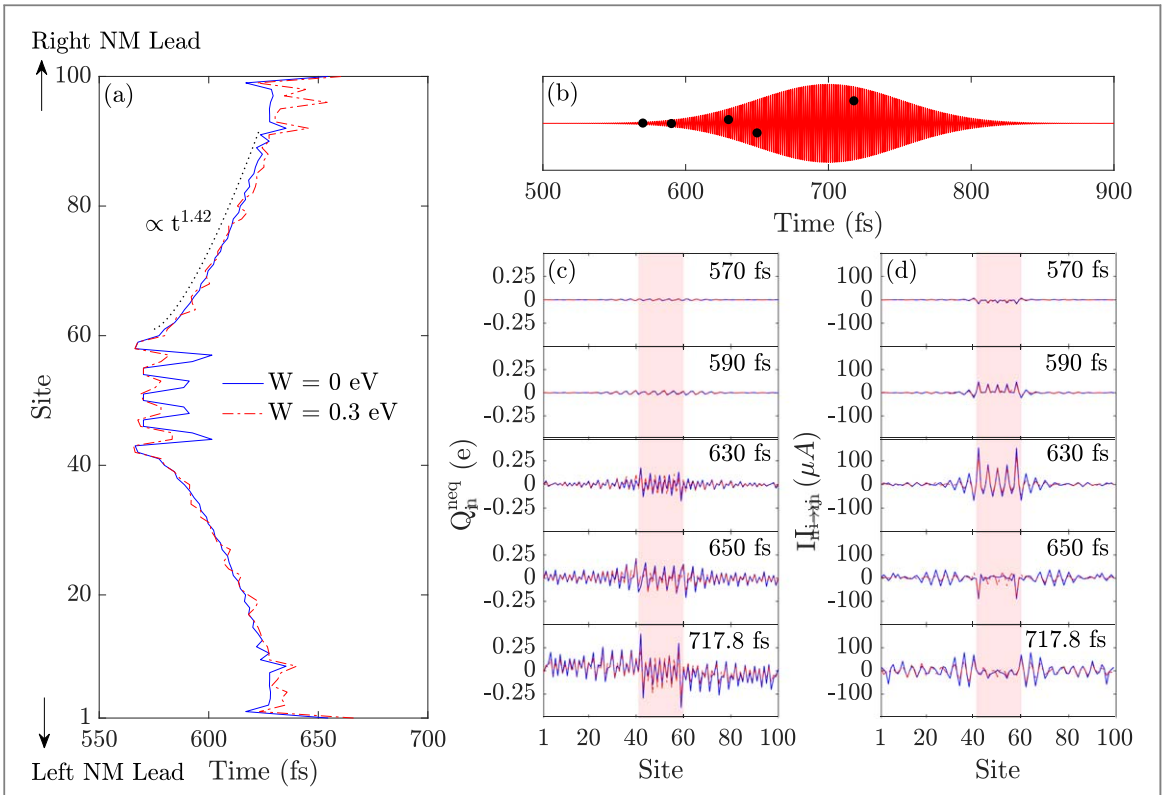

Figure 5. (a) Spatio-temporal profile of nonequilibrium charge $Q_n^{neq}(t)$ in equation (5) induced by femtosecond light pulse shown in panel (b)—of duration $\sigma_{light} = 50$ fs, center frequency $\hbar\Omega = 3.2$ eV and maximum amplitude $z_{max} = 0.5$—irradiating $N_{RM}^{light} = 20$ sites in the middle of a gapped device in figure 1 composed of $N_{RM} = 100$ sites. The curves in (a) trace sites where $|Q_n^{neq}(t)|$ at time t reaches 5% of the maximum value induced (at $t = 717.8$ fs in panel (c)) within the irradiated region. Spatial profile at selected times, marked by black dots in panel (b), for: (c) $Q_n^{neq}(t)$; and (d) local bond photocurrent $I_{n\to m}(t)$ between sites of Rice–Mele TB chain. In panels (a), (c) and (d), solid lines are for clean ($W = 0$ eV) and dash–dot lines are for disordered ($W = 0.3$ eV) Rice–Mele TB chain. Dotted line in panel (a) represents a power-law fitting of the solid curve in the same panel. The two movies depicting evolution of $I_{n\to m}(t)$ at all times in clean and diffusive two-terminal devices are provided in the supplemental materials (see footnote 6). The Fermi energy of electrons in the NM leads is chosen as $E_F = 0$ eV.

only in response to polarized light. Thus, the nonzero polarization vector is required to generate DC component of photocurrent in response to unpolarized light, albeit larger polarization does not always imply a larger photocurrent [14, 17].

However, these arguments do not consider realistic devices in two-terminal geometry for which the theory of nonadiabatic quantum charge pumping [39–41] predicts how leads made of different materials, or identical leads and static on-site potentials within the central region [42], break the left–right symmetry of the device structure to generate nonzero DC component of photocurrent in response to unpolarized light. We confirm the former possibility in figure 4(d) by using TB chain of finite length with uniform hoppings and zero on-site potential as the central region of Device 3 in figure 4(e). This is irradiated by light pulses of different polarizations (+ sign denotes polarization along the TB chain toward the right NM lead and − sign denotes polarization in the opposite direction), while the left–right symmetry of the device is broken by using two different NM leads. This generates photocurrent $I_L^+(t) + I_L^-(t)$ in response to unpolarized light with *nonzero* DC component $\propto \Omega^2$, as demonstrated in figure 4(d).

3.3. Superballistic spreading of photoexcited charge carriers

Motivated by very recent experiments [10, 11], exploring position dependence of photocurrent induced by applying CW light across the device or its temporal waveform induced by femtosecond light pulse, we examine spatial profiles of nonequilibrium charge (figure 5(c)), $Q_i^{neq}(t)$ in equation (5), and local bond current (figure 5(d)), $I_{n\to m}(t)$ in equation (8), at different times selected (figure 5(b)) within the duration of femtosecond light pulse. In addition, movies depicting spatial profile of $I_{n\to m}(t)$ at all times are provided in the supplemental materials[6]. Both $Q_n^{neq}(t)$ and $I_{n\to m}(t)$ profiles show that at the beginning of the pulse ($t = 570$ fs in figure 5) they are localized within the irradiated region composed of middle $N_{RM}^{light} = 20$ sites within $N_{RM} = 100$ sites Rice–Mele TB chain in figure 1. At later times, they propagate along non-irradiated region and are eventually collected by the NM leads.

To understand how fast the spreading of nonequilibrium charge is toward the NM leads, we analyze spatio-temporal profiles depicted in figure 5(a) which trace those sites of clean or disordered Rice–Mele TB chain where absolute value $|Q_i^{\rm neq}(t)|$ at time t reaches 5% (other cutoffs can be used without changing the conclusion) of the maximum value generated (at $t = 717.8$ fs in panel (c)) within the irradiated region. Thus, upper and lower curve in figure 5(a) can be viewed as the displacement of $Q_i^{\rm neq}$ toward the right or left NM lead, respectively. The scaling of the displacement with time, $\sim t^{\nu}$, can be analyzed akin to variance spreading of optical [43, 44] or quantum [45] wave packets or classical Brownian particle [46]: $\nu = 1$ signifies ballistic propagation in uniform lattices; $\nu = 0.5$ or $\nu = 0$ signifies diffusion or Anderson localization in disordered lattices, respectively; and subdiffusion ($0 < \nu < 0.5$) or superdiffusion ($0.5 < \nu < 1$) are also possible in some quasiperiodic lattices [47]. Surprisingly, we find $\nu = 1.42(11)$ in the case of clean Rice–Mele TB chain and $\nu = 1.28(15)$ in the case of the diffusive one, which demonstrates *superballistic* spreading of photoexcited nonequilibrium electrons.

We note that superballistic spreading of optical wave packets, within certain transient time frame, has been observed experimentally in disordered static [43] and temporally fluctuating [44] photonic lattices. The far-from-equilibrium quantum electron system studied in figure 5 does share some features with the latter case. The superballistic transport of photoexcited nonequilibrium charge carriers unveiled in figure 5, which evolve quantum-coherently and are largely insensitive to scattering off impurities, is remarkably different from photoexcited carriers in conventional *pn*-junction solar cells where they travel toward the leads via drift-diffusive transport requiring to manipulate their mobilities for efficient DC photocurrent extraction. The insensitivity to impurities of superballistic propagation of quantum-coherent shift current in figure 5 can explain the central result of experiments in [10] observing robust transport of photoexcited carriers without decay over surprisingly long distances $\sim 100\ \mu$m.

3.4. Diagonal versus off-diagonal elements of time-dependent nonequilibrium density matrix

Experimentally, the ballistic and shift contributions to BPVE can be distinguished by performing Hall effect measurements because ballistic current is sensitive to external magnetic field and shift current is not [4, 9]. Theoretically, the quantum-mechanical nature of shift current is encoded by the off-diagonal elements [24, 25] of $\boldsymbol{\rho}^{\rm neq}(t)$, in contrast to ballistic current arising from its diagonal elements [24, 25]. However, standard theoretical analysis is performed for infinite periodic crystals, which has lead to confusion [48] about how to identify shift current of carriers which are not illuminated by light [10]. The preferred basis [49] for analyzing quantum coherence encoded in the off-diagonal elements of the density matrix is typically the real-space basis, so akin to 'total site coherence' of [50] we define the following sum of amplitudes of the off-diagonal elements of $\boldsymbol{\rho}^{\rm neq}(t)$ in the basis of states $|n\rangle$

$$\chi_{\rm neq}^{\rm NIR(IR)}(t) = \frac{\sum_{n\neq m}|\langle n|\hat{\rho}^{\rm neq}(t) - \hat{\rho}^{\rm eq}|m\rangle|}{\sum_{n\neq m}\langle n|\hat{\rho}^{\rm eq}|m\rangle|} \times 100, \tag{11}$$

where sites $n \neq m$ belong to irradiated (IR) or non-irradiated (NIR) by the light pulse region of the Rice–Mele TB chain. This sum actually gives relative change (as a percent) of off-diagonal matrix elements with respect to the same matrix elements of the equilibrium density matrix $\boldsymbol{\rho}^{\rm eq}$. For comparison, we also define the sum of amplitudes of the diagonal elements of $\boldsymbol{\rho}^{\rm neq}(t)$

$$\xi_{\rm neq}^{\rm NIR(IR)}(t) = \frac{\sum_{n}|\langle n|\hat{\rho}^{\rm neq}(t) - \hat{\rho}^{\rm eq}|n\rangle|}{\sum_{n}\langle n|\hat{\rho}^{\rm eq}|n\rangle|} \times 100, \tag{12}$$

so that $\chi_{\rm neq}(t)^{\rm NIR(IR)} \gg \xi_{\rm neq}^{\rm NIR(IR)}(t)$ signifies processes which involve quantum coherence or superposed states. Figure 6 shows that relative change of the diagonal elements (figures 6(a), (c)) of the density matrix upon transition from equilibrium to nonequilibrium is $\lesssim 1\%$, in both irradiated and non-irradiated regions of Rice–Mele TB chain. On the other hand, relative change of the off-diagonal elements (figures 6(b), (d)) reaches 100%.

We also perform analysis of matrix elements of $\boldsymbol{\rho}^{\rm neq}(t)$ in the basis of Bloch states. For this purpose, we diagonalize Hamiltonian in equation (2) for a finite-length Rice–Mele TB chain of $N_{\rm RM} = 100$ sites with periodic boundary conditions and no light pulse applied. This gives eigenstates, $\hat{H}_{\rm RM}|E_q\rangle = E_q|E_q\rangle$, where we select those $|E_q\rangle$ within each two-dimensional eigensubspace which correspond to propagating Bloch states. Figure 6(e) plots time dependence of nonequilibrium charge $Q_{100}^{\rm neq}(t)$ in equation (5) at site $n = 100$ which is connected to the right NM lead and not irradiated by the light pulse. Figure 6(f) shows contribution to $Q_{100}^{\rm neq}(t)$ from the off-diagonal *interband* matrix elements $\langle E_q|\hat{\rho}^{\rm neq}(t) - \hat{\rho}^{\rm eq}|E_r\rangle$, where $E_q \neq E_r$ belong to different bands. Similarly, figure 6(h) shows contribution from the off-diagonal *intraband* matrix elements where $E_q \neq E_r$ belong to the same (valence or conduction) band. The off-diagonal intraband contribution in figure 6(h) is almost exactly canceled by the diagonal contribution (for which $E_q = E_r$) in figure 6(g).Thus, this reveals that photoexcited nonequilibrium charge density far away from irradiated region is governed *solely* by quantum coherence of superposed electron and whole wavefunctions.

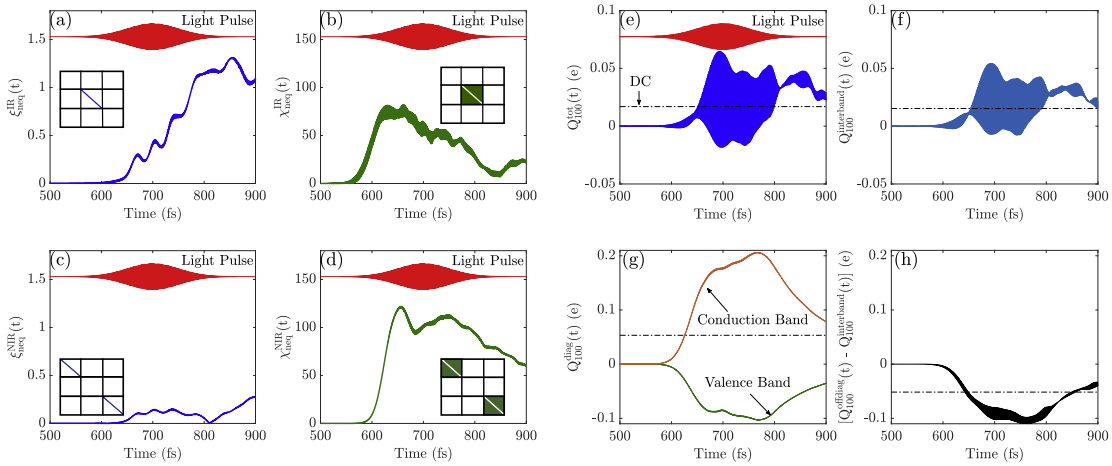

Figure 6. Time dependence of sum of amplitudes (equations (11) and (12)) of (a) the diagonal elements of nonequilibrium density matrix in the site representation, $\langle n|\hat{\rho}^{\rm neq}|m\rangle$, $n \neq m$; and (b) the off-diagonal elements of nonequilibrium density matrix in the site representation, $\langle n|\hat{\rho}^{\rm neq}|n\rangle$, for sites which are irradiated by the light pulse. Panels (c) and (d) show the same quantities for sites which are *not* irradiated by the light pulse, and insets in panels (a)–(d) illustrate matrix elements of $\hat{\rho}^{\rm neq}$ that are summed. The pulse—of duration $\sigma_{\rm light} = 50$ fs, center frequency $\hbar\Omega = 3.2$ eV and maximum amplitude $z_{\rm max} = 0.5$—irradiates $N_{\rm RM}^{\rm light} = 20$ sites of Rice–Mele gapped device in figure 1 of length $N_{\rm RM} = 100$ sites. Time dependence of: (e) total charge density $Q_{100}^{\rm tot}$ at the last site of Rice–Mele TB chain which is not irradiated by light pulse and it is attached to the first site of the right NM lead; (f) contribution to $Q_{100}^{\rm tot}$ generated by the off-diagonal interband elements of nonequilibrium density matrix, $\langle E_q|\hat{\rho}^{\rm neq} - \hat{\rho}^{\rm eq}|E_r\rangle$ with $E_q \neq E_r$ belonging to different bands; (g) contribution generated by the diagonal elements, $\langle E_q|\hat{\rho}^{\rm neq} - \hat{\rho}^{\rm eq}|E_r\rangle$; and (h) contribution generated by the off-diagonal elements, $\langle E_q|\hat{\rho}^{\rm neq} - \hat{\rho}^{\rm eq}|E_r\rangle$ with $E_q \neq E_r$, but belonging to the same band. The dash–dot line in panels (e)—(h) denotes the respective DC component. The Fermi energy of electrons in the NM leads is chosen as $E_F = 0$ eV.

4. Conclusions

Traditional theoretical analyses of photocurrent in noncentrosymmetric systems have been confined to perturbative treatment of an infinite periodic crystal homogeneously irradiated by continuous wave light. These assumptions are at odds with recent experiments where femtosecond light pulses are applied locally and propagation of photocurrent is studied away from the irradiated region. Furthermore, possibly high intensities of light make it desirable to include higher-order processes that would be naturally accounted for via a nonperturbative approach. Here we make a leap in the theoretical description by moving from perturbative to nonperturbative, and by moving the focus from the bulk material to a realistic device geometry perspective. Specifically, the nonperturbative TDNEGF approach employed in this study makes it possible to analyze spatio-temporal dynamics of photocurrent in realistic devices attached to external leads and exposed to either CW or pulse light of arbitrary intensity. We predict: subgap photocurrent generated by two-photon absorption mechanism; above the gap photocurrent generated by one-photon absorption mechanism; and its superballistic propagation away from irradiated region in *both* clean and diffusive (for conventional DC charge transport) systems. Importantly, we demonstrate that beyond the traditional target materials (i.e. noncentrosymmetric materials with nonzero polarization vector), a much broader class of systems can be explored to optimize the photocurrent in response to unpolarized light (as relevant for photovoltaic applications). The key requirement defining this broader class of systems is the same as for nonadiabatic quantum charge pumping—broken left–right symmetry of the device structure. For example, it is sufficient to take a two-dimensional material (even non-polar) which interacts with light strongly [51, 52] and attach it to two electrodes made of different metals in order to enable quantum-coherent shift current generation with nonzero DC component even when irradiating light is unpolarized.

Acknowledgments

UB, BSP and BKN were supported by NSF grant No. CHE 1566074. PP was supported by ARO MURI Award No. W911NF-14-0247. LEFFT was supported by FondeCyT grant No. 1170917 (Chile). HI and NN were supported by Japan Society for the Promotion of Science KAKENHI (grants No. JP16H06717 and JP26103006); ImPACT Program of Council for Science, Technology and Innovation (Cabinet office, Government of Japan, 888176); and CREST, Japan Science and Technology (grant no. JPMJCR16F1). This work used the Extreme Science and Engineering Discovery Environment (XSEDE), which is supported by NSF grant No. ACI-1548562.

ORCID iDs

U Bajpai https://orcid.org/0000-0002-1974-0450
B K Nikolić https://orcid.org/0000-0002-5793-7764
L E F Foa Torres https://orcid.org/0000-0002-6319-9593

References

[1] Polman A and Atwater H A 2012 Photonic design principles for ultrahigh-efficiency photovoltaics *Nat. Mater.* **11** 175
[2] Sturman B S I and Fridkin V M 1992 *Photovoltaic and Photorefractive Effects in Noncentrosymmetric Materials* (Philadelphia: Gordon and Breach)
[3] Král P, Mele E J and Tománek D 2000 Photogalvanic effects in heteropolar nanotubes *Phys. Rev. Lett.* **85** 1512
[4] Zenkevich A, Matveyev Yu, Maksimova K, Gaynutdinov R, Tolstikhina A and Fridkin V 2014 Giant bulk photovoltaic effect in thin ferroelectric $BaTiO_3$ films *Phys. Rev.* B **90** 161409(R)
[5] Osterhoudt G B *et al* 2019 Colossal bulk photovoltaic effect in a type-I Weyl semimetal *Nat. Mater.* **March 2019** 1–5
[6] Daranciang D *et al* 2012 Ultrafast photovoltaic response in ferroelectric nanolayers *Phys. Rev. Lett.* **108** 087601
[7] Priyadarshi S, Pierz K and Bieler M 2012 All-optically induced ultrafast photocurrents: beyond the instantaneous coherent response *Phys. Rev. Lett.* **109** 216601
[8] Wachter G, Sato S A, Floss I, Lemell C, Tong X-M, Yabana K and Burgdörfer J 2015 Controlling ultrafast currents by the nonlinear photogalvanic effect *New J. Phys.* **17** 123026
[9] Spanier J E *et al* 2016 Power conversion efficiency exceeding the Shockley–Queisser limit in a ferroelectric insulator *Nat. Photon.* **10** 611
[10] Nakamura M, Horiuchi S, Kagawa F, Ogawa N, Kurumaji T, Tokura Y and Kawasaki M 2017 Shift current photovoltaic effect in a ferroelectric charge-transfer complex *Nat. Commun.* **8** 281
[11] Ogawa N, Sotome M, Kaneko Y, Ogino M and Tokura Y 2017 Shift current in the ferroelectric semiconductor SbSI *Phys. Rev.* B **96** 241203(R)
[12] Young S M and Rappe A M 2012 First principles calculation of the shift current photovoltaic effect in ferroelectrics *Phys. Rev. Lett.* **109** 116601
[13] Tan L Z and Rappe A M 2016 Enhancement of the bulk photovoltaic effect in topological insulators *Phys. Rev. Lett.* **116** 237402
[14] Tan L Z, Zheng F, Young S M, Wang F, Liu S and Rappe A M 2016 Shift current bulk photovoltaic effect in polar materials–Hybrid and oxide perovskites and beyond *NPJ Comput. Mater.* **2** 16026
[15] Cook A M, Fregoso B M, de Juan F, Coh S and Moore J E 2017 Design principles for shift current photovoltaics *Nat. Commun.* **8** 14176
[16] Rangel T, Fregoso B M, Mendoza B S, Morimoto T, Moore J E and Neaton J B 2017 Large bulk photovoltaic effect and spontaneous polarization of single-layer monochalcogenides *Phys. Rev. Lett.* **119** 067402
[17] Fregoso B M, Morimoto T and Moore J E 2017 Quantitative relationship between polarization differences and the zone-averaged shift photocurrent *Phys. Rev.* B **96** 075421
[18] Ishizuka H and Nagaosa N 2017 Local photo-excitation of shift current in noncentrosymmetric systems *New J. Phys.* **19** 033015
[19] Morimoto T and Nagaosa N 2016 Topological nature of nonlinear optical effects in solids *Sci. Adv.* **2** e1501524
[20] Nagaosa N and Morimoto T 2017 Concept of quantum geometry in optoelectronic processes in solids: application to solar cells *Adv. Mater.* **29** 1603345
[21] Xu S-Y *et al* 2018 Electrically switchable Berry curvature dipole in the monolayer topological insulator WTe_2 *Nat. Phys.* **14** 900
[22] Ma Q *et al* 2017 Direct optical detection of Weyl fermion chirality in a topological semimetal *Nat. Phys.* **13** 842
[23] Zhang Y, Ishizuka H, van den Brink J, Felser C, Yan B and Nagaosa N 2018 Photogalvanic effect in Weyl semimetals from first principles *Phys. Rev.* B **97** 241118(R)
[24] von Baltz R and Kraut W 1981 Theory of the bulk photovoltaic effect in pure crystals *Phys. Rev.* B **23** 5590
[25] Král P 2000 Quantum kinetic theory of shift-current electron pumping in semiconductors *J. Phys.: Condens. Matter* **12** 4851
[26] Sipe J E and Shkrebtii A I 2000 Second-order optical response in semiconductors *Phys. Rev.* B **61** 5337
[27] Fathpour S, Tsia K and Jalali B 2007 Two-photon photovoltaic effect in silicon *IEEE J. Quantum Electron.* **43** 1211
[28] Ma J, Chiles J, Sharma Y D, Krishna S and Fathpour S 2014 Two-photon photovoltaic effect in gallium arsenide *Opt. Lett.* **39** 5297
[29] Stefanucci G and van Leeuwen R 2013 *Nonequilibrium Many-Body Theory of Quantum Systems: a Modern Introduction* (Cambridge: Cambridge University Press)
[30] Gaury B, Weston J, Santin M, Houzet M, Groth C and Waintal X 2014 Numerical simulations of time-resolved quantum electronics *Phys. Rep.* **534** 1
[31] Asbóth J K, Oroszlány L and Pályi A 2016 *A Short Course on Topological Insulators: Band Structure and Edge States in One and Two Dimensions* (Cham: Springer)
[32] Croy A and Saalmann U 2009 Propagation scheme for nonequilibrium dynamics of electron transport in nanoscale devices *Phys. Rev.* B **80** 245311
[33] Popescu B S and Croy A 2016 Efficient auxiliary-mode approach for time-dependent nanoelectronics *New J. Phys.* **18** 093044
[34] Nikolić B K, Zârbo L P and Souma S 2006 Imaging mesoscopic spin Hall flow: spatial distribution of local spin currents and spin densities in and out of multiterminal spin–orbit coupled semiconductor nanostructures *Phys. Rev.* B **73** 075303
[35] Areshkin D A and Nikolić B K 2010 Electron density and transport in top-gated graphene nanoribbon devices: first-principles Green function algorithms for systems containing a large number of atoms *Phys. Rev.* B **81** 155450
[36] Mahfouzi F, Fabian J, Nagaosa N and Nikolić B K 2012 Charge pumping by magnetization dynamics in magnetic and semimagnetic tunnel junctions with interfacial Rashba or bulk extrinsic spin–orbit coupling *Phys. Rev.* B **85** 054406
[37] Golub L E and Ivchenko E L 2011 Shift photocurrent induced by two-quantum transitions *J. Exp. Theor. Phys.* **112** 152
[38] Bhatnagar A, Chaudhuri A R, Kim Y H, Hesse D and Alexe M 2013 Role of domain walls in the abnormal photovoltaic effect in $BiFeO_3$ *Nat. Commun.* **4** 2835
[39] Vavilov M G, Ambegaokar V and Aleiner I L 2001 Charge pumping and photovoltaic effect in open quantum dots *Phys. Rev.* B **63** 195313
[40] Moskalets M and Büttiker M 2002 Floquet scattering theory of quantum pump *Phys. Rev.* B **66** 205320
[41] Foa Torres L E F 2005 Mono-parametric quantum charge pumping: interplay between spatial interference and photon-assisted tunneling *Phys. Rev.* B **72** 245339

[42] Chen S-H, Chang C-R, Xiao J Q and Nikolić B K 2009 Spin and charge pumping in magnetic tunnel junctions with precessing magnetization: a nonequilibrium Green function approach *Phys. Rev.* B **79** 054424
[43] Stützer S, Kottos T, Tünnermann A, Nolte S, Christodoulides D N and Szameit A 2013 Superballistic growth of the variance of optical wave packets *Opt. Lett.* **38** 4675
[44] Levi L, Krivolapov Y, Fishman S and Segev M 2012 Hyper-transport of light and stochastic acceleration by evolving disorder *Nat. Phys.* **8** 912
[45] Zhang Z, Tong P, Gong J and Li B 2012 Quantum hyperdiffusion in one-dimensional tight-binding lattices *Phys. Rev. Lett.* **108** 070603
[46] Bouchaud J-P and Georges A 1990 Anomalous diffusion in disordered media: statistical mechanisms, models and physical applications *Phys. Rep.* **195** 127
[47] Abe S and Hiramoto H 1987 Fractal dynamics of electron wave packets in one-dimensional quasiperiodic systems *Phys. Rev.* A **36** 5349
[48] Fridkin V M and Spanier J E 2018 Reconsidering evidence of shift current in a ferroelectric charge-transfer complex (arXiv:1802.05658)
[49] Schlosshauer M 2005 Decoherence, the measurement problem, and interpretations of quantum mechanics *Rev. Mod. Phys.* **76** 1267
[50] Hoyer S, Sarovar M and Whaley K B 2010 Limits of quantum speedup in photosynthetic light harvesting *New J. Phys.* **12** 065041
[51] Xia F, Wang H, Xiao D, Dubey M and Ramasubramaniam A 2014 Two-dimensional material nanophotonics *Nat. Photon.* **8** 899
[52] Chen S and Shi G 2017 Two-dimensional materials for halide perovskite-based optoelectronic devices *Adv. Mater.* **29** 1605448